ELSEVIER

Review

An improved numerical method for strong coupling of excitation and contraction models in the heart

Steven A. Niederer[a,b], Nicolas P. Smith[a,b],*

[a]*Bioengineering Institute, University of Auckland, Auckland, New Zealand*
[b]*Computing Laboratory, University of Oxford, Wolfson Building, Parks Road, Oxford, OX1 3QD, UK*

Abstract

Quantifying the interactions between excitation and contraction is fundamental to furthering our understanding of cardiac physiology. To date simulating these effects in strongly coupled excitation and contraction tissue models has proved computationally challenging. This is in part due to the numerical methods implemented to maintain numerical stability in previous simulations, which produced computationally intensive problems. In this study, we analytically identify and quantify the velocity and length dependent sources of instability in the current established coupling method and propose a new method which addresses these issues. Specifically, we account for the length and velocity dependence of active tension within the finite deformation equations, such that the active tension is updated at each intermediate Newton iteration, within the mechanics solution step. We then demonstrate that the model is stable and converges in a three-dimensional rod under isometric contraction. Subsequently, we show that the coupling method can produce stable solutions in a cube with many of the attributes present in the heart, including asymmetrical activation, an inhomogeneous fibre field and a nonlinear constitutive law. The results show no instabilities and quantify the error introduced by discrete length updates. This validates our proposed coupling framework, demonstrating significant improvement in the stability of excitation and contraction simulations.
© 2007 Elsevier Ltd. All rights reserved.

Keywords: Coupled electromechanics; Cardiac; Stability; Three dimensional; Computational model

Contents

*Corresponding author. Tel.: +44 (0) 1865 610669; fax: +44 (0) 1865 273839.
E-mail address: nic.smith@comlab.ox.ac.uk (N.P. Smith).

1. Introduction

During each beat the heart is electrically stimulated, Ca^{2+} is released from intracellular stores, sarcomeres are activated, tension is generated and the heart contracts. However, this apparently ordered series of events is controlled by a complex web of feedback loops which contribute to the maintenance of systemic blood flow and pressure at desired levels. Within a cardiac cell tension is generated within sarcomeres that are activated by the $[Ca^{2+}]_i$ transient, resulting in deformation. Coupling mechanisms between electrophysiology and mechanics are key contributors to controlling this series of events. The deformation can alter stretch activated channels (Zeng et al., 2000), stretch dependent regulation of ryanodine receptors (Petroff et al., 2001), Na^+-H^+ exchange (Alvarez et al., 1999) and $Cl^--HCO_3^-$ exchange (Alvarez et al., 2001) and tension dependent Ca^{2+} buffering (Fuchs et al., 1988). All these mechanisms contribute to changes in cardiac electrophysiology and Ca^{2+} handling and hence feedback to tension development and deformation.

Quantifying these interactions and feedback loops between activation and contraction and how they affect global pump function is essential in our understanding of the heart. However, as outlined above, the interactions are complex, occur over a broad range of spatial and temporal scales, and are hence challenging to study experimentally at the whole heart scale. Mathematical models of coupled electromechanics provide a framework to coalesce the relevant experimental data to further our understanding of these interactions. Yet, the development and implementation of numerical and computational methods to efficiently and effectively couple complex biophysically based cell models to three-dimensional cardiac electromechanics heart simulations remains challenging.

Currently the majority of coupled electromechanics models fall into one of two categories, namely weakly and strongly coupled (Kerckhoffs et al., 2006). In simulations using a weak coupling method the electrical activation time is calculated at each point in the heart through Eikonal mapping (Tomlinson et al., 2002) or the solution of the mono or bi domain equations (Plonsey and Barr, 1984). Subsequently, the activation time and/or $[Ca^{2+}]_i$ transient is used as an input into a cellular model of active tension which is embedded in a spatially distributed tissue model governed by the finite deformation equations (Kerckhoffs et al., 2005; Usyk and McCulloch, 2003). The weak coupling method implicitly assumes that the coupling effects between deformation and electrophysiology outlined above are nominal and can hence be ignored. However, this assumption is controversial in light of experimental studies, which have shown a strong link between electrophysiology and mechanics (Lab, 1999), as outlined above, with changes in length dependent mechanisms affecting Ca^{2+} buffering (Fuchs and Wang, 1996), $[Na^+]_i$ (Alvarez et al., 1999) and action potential duration (Zeng et al., 2000). The alternate method is to use strong coupling, where the electrical activation, active tension and deformation are calculated at the same time and the feedback mechanisms between them are included in the underlying numerical solution to the governing equations. However, this temporal coupling has produced decreased numerical stability in current implementations of strong coupling,

which is only managed with a significant increase in computational load. This has led to strongly coupled models only being solved using simplified cell models (Nickerson et al., 2005) or in tissue models with reduced dimensionality (Smith et al., 2003).

In this study, we identify sources of numerical instability in strongly coupled problems and propose new methods to overcome the problems encountered in previous implementations. We begin with a brief overview of the numerical methods employed to simulate electrophysiology, active contraction and mechanics. The current method used in strongly coupled simulations is discussed, followed by a quantitative discussion of the sources of instability. We then quantify and propose a solution to each source of instability, providing specific examples using models developed within our group. Following this, a convergence analysis for a coupled electromechanics simulation in a simplified ($\approx$ rat papillary, Loiselle, 1982) geometry is performed. The model uses a biophysically detailed electrophysiology and active contraction cell model coupled with a transversely isotropic myocardium constitutive law. A demonstration of a cube containing an inhomogeneous fibre fields is also provided to demonstrate the stability of the proposed coupling method in complex three-dimensional geometries. From these simulations we quantify the computational efficiency and stability for strongly coupled electromechanics simulations.

2. Modeling electromechanics

Models of coupled electromechanics require a description of the electrical activation of the tissue, the active tension (T_a) generated by the sarcomeres following activation and the resulting deformation caused by the T_a field. We now provide brief overviews of the methods employed to describe each of these models, focusing on the inclusion of T_a in deformation models which is fundamental to the method proposed in this study.

2.1. Electrophysiology

Three-dimensional biophysically based cardiac electrophysiology models are predominately separated into two components, transmembrane current (I_{ion}) and electrical propagation. Transmembrane current is calculated in a cell model described by a system of ordinary differential equations (ODEs) (Eq. (1)):

$$I_{ion} = g(y, t),$$
$$\frac{dy}{dt} = f(y, t). \tag{1}$$

Depending on the complexity, the cell model will calculate the change in cellular and sub-cellular ionic concentrations, the transient cell membrane conductivity and the tension generated by the myofilaments. Electrical propagation is described by the bidomain equations (Schmitt, 1969), which model the heart as two interpenetrating domains with the flux between the two domains being provided by I_{ion}, calculated in the cell model (Eq. (1)). In coupled electromechanics models, electrical propagation is typically solved on a finer mesh (referred to as a grid) than the mechanics finite element mesh. Hence the grid is defined within the material space of the mechanics finite element mesh, which describes the geometry of the heart, allowing the grid to deform as the heart contracts (Smith et al., 2003; Buist et al., 2003).

2.2. Active contraction

In biophysically detailed models T_a is calculated from equations representing the development of tension from cellular cross bridge cycling. Due to the computational intensity of the alternatives (Rice et al., 2003; Huxley, 1957) T_a has been typically modeled using ODEs (Smith et al., 2003; Nickerson et al., 2005; Kerckhoffs et al., 2005; Sermesant et al., 2006; Watanabe et al., 2004) in tissue simulations. Most models of coupled electromechanics defined by system of ODEs can be described generically using functions h and f defined in Eq. (2):

$$T_a = h(\lambda, \dot{\lambda}, y, t), \quad \frac{dy}{dt} = f(T_a, \lambda, \dot{\lambda}, y, t), \tag{2}$$

where λ is the fibre strain ratio, $\dot{\lambda}$ is the strain rate, y is the vector of myofilament and electrophysiology state variables, f is an extension of f from Eq. (1), now with mechanics state variables included and t is time. The addition of $\dot{\lambda}$, λ and T_a to f from Eq. (1) in Eq. (2) provide the cellular excitation contraction coupling mechanisms which are included to varying degrees in cellular cardiac electromechanics models. The components of y pertaining to the myofilaments represent thin filament and cross bridge states within the cell.

2.3. Mechanics

To account for the complex geometry and fibre structure of the heart, the mechanical constitutive laws describing the myocardium are inhomogeneous, anisotropic and nonlinear. These attributes have led to the application of the finite element method to solve the finite deformation elasticity equations and calculate deformation in the heart in the presence of ventricular pressure and/or T_a fields (Nash and Hunter, 2000; Yin, 1981). Finite deformation elasticity is composed of four components, namely: kinetic relations, equations of motion, constitutive relations and boundary conditions. The resulting equilibrium equations are then discretized using the finite element method and solved using Newton iterations. For the purpose of providing the necessary context for the instability sources, each of the four components are now briefly outlined.

The kinematic relations describe the mapping of material points between the deformed ($\mathbf{x}$) and undeformed ($\mathbf{X}$) states using strain tensors. The strain tensors, given in Eq. (3), are used in the definition of the material constitutive law (Eq. (6)) and the equilibrium equations (Eq. (4)) described below:

$$F_{ij} = \frac{\partial x_i}{\partial X_j}, \quad \mathbf{E} = \frac{1}{2}(\mathbf{F}^\mathrm{T}\mathbf{F} - \mathbf{I}), \tag{3}$$

where $\mathbf{F}$ is the deformation gradient tensor, $\partial x_i/\partial X_j$ is the change in length between the deformed and undeformed state and $\mathbf{E}$ is the Green strain tensor (Malvern, 1969). In the heart these strain tensors are also used to define the assumed incompressibility constraint (Nash and Hunter, 2000).

The equations of motion describe the conservation of mass and the conservation of linear and angular momentum. These are combined to provide a relationship ($\mathbf{G}$) between the unknown internal stress and strain tensor fields (left-hand side of Eq. (4)) and the known body forces, inertia and boundary conditions (right-hand side of Eq. (4)), referred to as the equilibrium equation (Eq. (4)) (Malvern, 1969):

$$\mathbf{G}(T^{\mathrm{MN}}, \mathbf{F}) = \mathbf{B}, \tag{4}$$

where T^{MN} is the second Piola–Kirchhoff stress referred to material axes M & N, which are typically aligned to micro-structural axes within the tissue (Nash and Hunter, 2000) and $\mathbf{B}$ is a lumped vector of body forces, inertia and boundary conditions.

To express $\mathbf{G}$ solely as a function of strain requires a description of the stress tensor (T^{MN}) as a function of strain ($\mathbf{E}$) or deformation gradient ($\mathbf{F}$) tensor components. This description of the material properties is provided by a constitutive law. In the heart T^{MN} is comprised of three components: a passive component (T_p), which describes the stress required to cause a given deformation of the passive myocardium and active component (T_a), representing the tension generated by cross bridge cycling within the sarcomeres. T_p is commonly described by the derivatives of a strain energy function with respect to the Green strain tensor ($\mathbf{E}$) (Schmid et al., 2006; Nash and Hunter, 2000; Costa et al., 1996). As already outlined above, T_a is typically calculated in a cell model (Eq. (2)) and is assumed to act in the fibre direction referenced to the deformed co-ordinates as an additional component of the Cauchy stress tensor Nash and Hunter (2000). T_a is calculated as a Cauchy stress (force per unit deformed area), however, for consistency with experimental data constitutive laws are typically referenced to a geometry based in the undeformed co-ordinate system. Thus, T_a must be converted to a second Piola–Kirchhoff stress using Eq. (5) (Malvern, 1969), before inclusion in the constitutive law:

$$\tilde{T}_a = \frac{\rho_0}{\rho}\mathbf{F}^{-1}T_a(\mathbf{F}^{-1})^\mathrm{T}, \tag{5}$$

where ρ_0 and ρ are the density in the undeformed and deformed states, respectively, and, $\tilde{T}_a$ and T_a are the active stress contributions to the second Piola–Kirchhoff and Cauchy stress tensors, respectively. For

isovolumetric materials $\rho_0/\rho = 1$. In the case of T_a acting in the fibre direction only $\mathbf{F}^{-1}T_a(\mathbf{F}^{-1})^{\mathrm{T}} = T_a\mathbf{C}^{-1}$, where $\mathbf{C} = \mathbf{F}^{\mathrm{T}}\mathbf{F}$. The constitutive relation is then defined by Eq. (6):

$$T^{\mathrm{MN}} = \frac{1}{2}\left(\frac{\partial W(E)}{\partial E_{\mathrm{MN}}} + \frac{\partial W(E)}{\partial E_{\mathrm{NM}}}\right) - pC^{\mathrm{MN}} + T_a C^{\mathrm{MN}}, \tag{6}$$

where W is the strain energy function and $C^{\mathrm{MN}} = C_{\mathrm{MN}}^{-1}$. W is typically defined by an orthotropic or transversely isotropic nonlinear constitutive law (Schmid et al., 2006; Nash and Hunter, 2000; Costa et al., 1996).

Finally, we calculate the boundary conditions, body forces and inertia terms that make up **B**. The components of the equilibrium equations (geometry, strain, stress, body force and boundary conditions) can now be approximated using the finite element method, providing a system of equations which are nonlinear functions of the components of strain. This nonlinear system of equations is then solved using Newton iterations, in a series of solutions of equations, to a linear approximation, in the form Ax = b. The final result is a strain field for the given boundary conditions and the T_a field, from which stress can be calculated as desired.

3. Strongly coupled solution methods

In previous strongly coupled models of active contraction T_a was calculated at the cellular level and passed to the mechanics problem, where T_a was included in the constitutive equation through Eq. (6) (Nickerson et al., 2005; Smith et al., 2003). The T_a value was fixed throughout the mechanics solution, hence we shall refer to this method as the *fixed* method. Fig. 1 schematically represents the path of the *fixed* method through the electromechanics coupling framework via labeled arrows 1–4. When implemented, the *fixed* method simulations are typically solved at two distinct time scales, one for the cell and one for the mechanics. The cell model representing T_a and electrophysiology is integrated at the cell time scale over the period of time between solutions of the mechanics model. T_a is then incorporated into the constitutive equation (Eq. (6)) (arrow 1, Fig. 1), boundary conditions are applied and mechanics are solved (arrow 2, Fig. 1) using the finite deformation equations with T_a constant at each Newton iteration. Having converged (arrow 3, Fig. 1), the
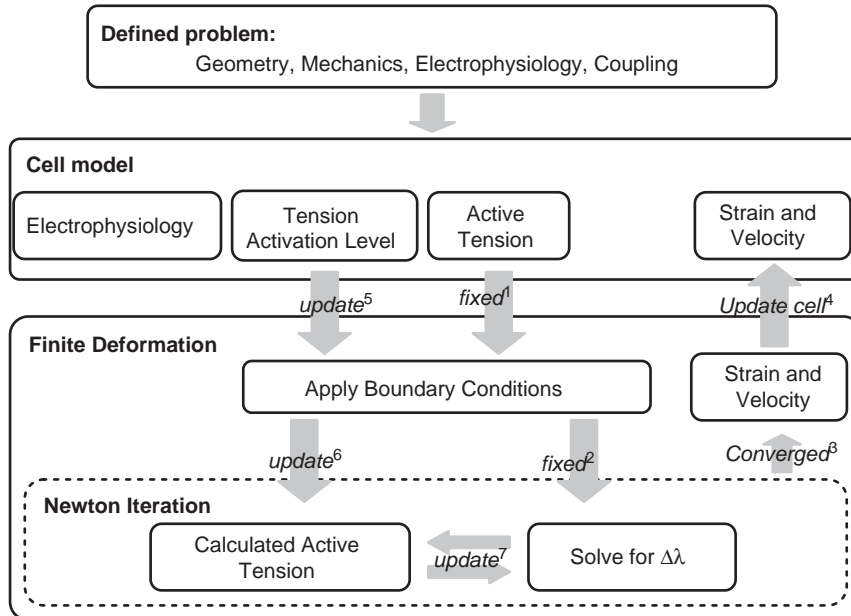

Fig. 1. Flow diagram outlining the processes and steps involved in solving a coupled electromechanics problem. The arrows either indicate a flow of information. The arrow labels indicate which coupling method (*fixed* or *update*) the arrows relate to (arrows 1,2,5–8) or provide a description of the algorithmic step (arrows 3,4).

length and velocity are then passed to the cell model (arrow 4, Fig. 1) and the process is repeated. It is relevant to note for the discussions below that within this schema T_a is dependent only on the converged solution at the previous time step. This effectively lags the coupling between the finite deformation solution and the calculation of T_a by one mechanics solution time step. The error introduced by this offset has been assumed minimal in the past and the *fixed* method has been the preferred method for solving large scale strongly coupled electromechanics problems (Kerckhoffs et al., 2006; Nickerson et al., 2005; Smith et al., 2003). A significant benefit of the *fixed* method is that it is easy to implement using existing electrophysiology and finite deformation codes. However, this implementation, as we show, has led to numerical instabilities, which significantly compromise stability and/or computational tractability. We now propose a new modeling framework, referred to as the *update* method, where T_a is updated during the mechanics solution step, which removes the sources of instabilitythat we identify below.

In the *update* method T_a is calculated within the cell model; however, a length and velocity independent level of tension activation ($\hat{T}$) is passed to the finite deformation equations as opposed to the T_a value (arrow 5, Fig. 1). Boundary conditions are then applied to the mechanics model (arrow 6, Fig. 1) and the model is discretized into a system of equations using the finite element method. The equations are solved using Newton's method, as noted above. The important difference is that during each Newton iteration the length and velocity dependence of active tension are accounted for within the solution of the mechanics problem. The active tension is updated at each intermediate strain field at each intermediate Newton iteration solution, at the same time that the T_p value at a given strain is calculated (arrow 7, Fig. 1). Following convergence (arrow 3, Fig. 1) the length and velocity field is passed to the cell model (arrow 4, Fig. 1) and the process repeats. This small modification is, as we will show, important in that it allows changes in active tension with length and velocity to be accounted for at each Newton iteration during the solution of the equilibrium equations.

4. Numerical instabilities

4.1. Length dependent instabilities

The *fixed* coupling method has instabilities caused by the length dependence of T_a. In a majority of cardiac contraction models, T_a is calculated from the product of an often linear strain dependent scalar representing filament overlap and a scalar representing the remaining model components, which account for how cross bridge transients and thin filament kinetics affect tension. This is typically described by a linear overlap function (α) such as Eq. (7) (Niederer et al., 2006; Hunter et al., 1998; Rice et al., 1999; Sachse et al., 2003; Vendelin et al., 2000):

$$\alpha = (1 + \beta_0(\lambda - 1)), \tag{7}$$

where β_0 is the length dependence of isometric tension and λ is the strain. The α function poses a problem as negative tensions occur for λ values below $1 - 1/\beta_0$. We shall refer to this critical strain value as λ_c. As λ reduces, T_a decreases and T_p increases, therefore there should be a length at which T_p balances T_a before T_a becomes negative, in the absence of external loads. By uncoupling the constitutive law from the T_a model, as in the *fixed* coupling method, λ values may be reached at intermediate Newton iterations during the solution of the equilibrium equation (Eq. (4)), which are less than λ_c, hence causing negative T_a values. Furthermore, in complex three-dimensional tissue simulations boundary conditions may be applied which force λ to be less than λ_c, regardless of the T_a value, again causing negative T_a values. These problems can be mitigated by reducing T_a to zero when λ is less than λ_c, however, as we now show oscillatory solutions will still occur.

Fig. 2 demonstrates schematically how oscillatory solutions occur for a one-dimensional fibre in the *fixed* coupling method and how the *update* removes them. Fig. 2 shows three second Piola–Kirchhoff stresses, the solution states and the strain (λ_c) beyond which T_a is set to zero to avoid it becoming negative. The second Piola–Kirchhoff stresses are calculated via Eq. (6) in the fibre direction as a function of strain. The solution states correspond to the solution following each Newton iteration. The dash-dotted line is T_p in the presence of no active tension. In this passive relation, as no external loads are being applied, strain is equal to the intercept of the dash-dotted line and $T_p = 0$ at $\lambda = 1$, hence the model is in the 'resting state'. Following an
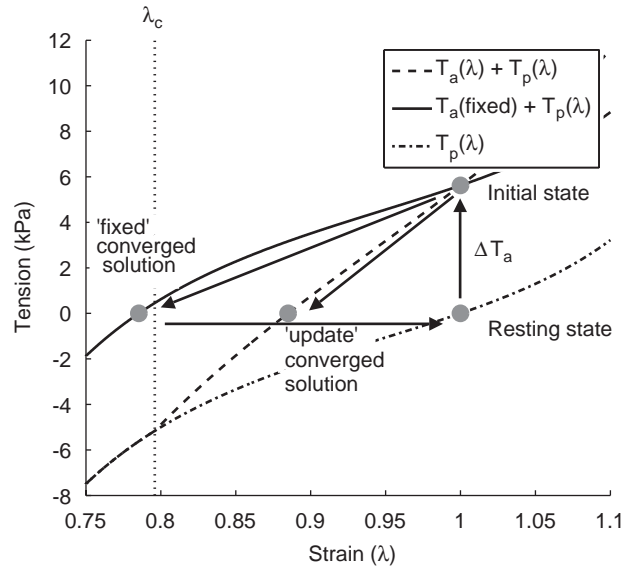
Fig. 2. Schematic diagram showing how the *fixed* coupling method causes length dependent instabilities. The three curves relate to the component of the second Piola–Kirchhoff stress tensor aligned with the fibres calculated from the constitutive law (Eq. (6)) in the absence of a T_a (dash-dotted line), in the presence of ΔT_a for a *fixed* coupling method (solid line) and in the presence of ΔT_a for the *update* coupling method (dashed line). The strain beyond which $T_a < 0$ is shown by the dotted line marked λ_c. The grey dots correspond to converged and intermediate solution states.

increase in T_a (ΔT_a) the model moves to the 'initial state'. At this point under the *fixed* method the strain solution will converge along the solid line to a '*fixed* converged solution', where T_p and T_a are equal. As the strain decreases during each Newton iteration the T_a value remains constant. The final strain is to the left of λ_c, such that when T_a is calculated again it will be equal to zero. In the next time step, T_a is calculated in the cell model using the λ value from the previous time step. As $\lambda < \lambda_c$ the new T_a is set to 0, hence the mechanics solution converges back to the 'resting state' with $\lambda = 1$. At the next time step the iterative solution will follow the same sequence of state values, which will then be the same as the first cycle of intermediate solutions. Thus, in one-dimensional problems, for the same ΔT_a, this cycle will continue indefinitely, regardless of the time between the solution of the finite deformation elasticity equations. If we do not assume that $T_a = 0$ for $\lambda < \lambda_c$, then negative tensions will be generated, leading to the paradoxical result of an increase in strain following an increase in compressive force, resulting in solution failure.

In the *update* method, the cell model passes a level of tension activation to the mechanics problem and the length dependent T_a (T_a in Eq. (6)) is recalculated at each Newton iteration, such that at the 'initial state' the problem converges along the dashed line (as opposed to the solid line) to reach the '*update* converged solution' and experiences no cyclical behaviour.

To quantify the conditions for the length dependent stability let us first consider a velocity independent T_a (Eq. (8)):

$$T_a = T_{\text{ref}}\hat{z}\alpha, \tag{8}$$

where T_{ref} is the isometric tension at $\lambda = 1$, $\hat{z}$ is a Ca^{2+} dependent measure of fractional activation and α is defined by Eq. (7). Under the *fixed* coupling method, following an increase in $\hat{z}$ the cell model is solved to give the new T_a at time t_{i+1} using the strain λ_i. In the case of a one-dimensional fibre the strain at t_{i+1} is then calculated using $T_p = -T_a$ (derived in the Appendix Eq. (34)) and the new T_a value giving Eq. (9):

$$T_p(\lambda_{i+1}) = -T_{\text{ref}}(1 + \beta_0(\lambda_i - 1))\hat{z}. \tag{9}$$

If we set T_a to be zero if strain is less than λ_c then Eq. (9) will converge if:

$$T_{\text{ref}}\hat{z} < -T_p(\lambda_c) \tag{10}$$

such that, if T_a is greater than the passive tension at λ_c then the mechanics solution will inevitably converge to the left of λ_c in Fig. 2 and enter into a cycle, as outlined above.

4.2. Velocity dependent instabilities

In addition to the length dependency issues resolved above, T_a in cardiac muscle is also highly velocity dependent. Hence, including these dependencies in models of coupled electromechanics must be considered. Velocity dependencies come from forcing cross bridges to unbind or moving tension generating cross bridges into stress free or high stress conformations. These dependencies are notable under isotonic contractions, sinusoidal perturbations or following rapid length changes. In models of contraction, velocity is accounted for in the form of a velocity dependent scale factor of T_a (Niederer et al., 2006; Hunter et al., 1998), a variable in cross bridge binding rates (Sachse et al., 2003; Razumova et al., 1999) or using a phenomenological representation (Taber et al., 1996).

Fig. 3 shows a second schematic of a one-dimensional coupled electromechanics simulation. In Fig. 3, T_p is shown as a function of strain (solid line). The negative of T_a is plotted, as strain determined at intermediate and converged solutions is calculated by the solution of $-T_a = T_p$ in a simplified one-dimensional fibre, as discussed below. T_a is shown as a function of strain at a low and a higher level of activation, caused by different concentrations of $[Ca^{2+}]_i$ (dotted and dash-dotted lines, respectively). With an increase in activation, resulting in the T_a curve shifting to the left (as we are referring to negative T_a) from state 1 (dotted line) to 2 (dash-dotted line) then an unstable solution may result within the *fixed* coupling framework. The start point for our schematic demonstration is at t_0 with strain (λ_0), velocity ($d\lambda_0/dt$) and active tension (T_0) at their initial states. In step 1, the cell model calculates the new active tension (T_1) at the new activation level at time t_1 using the strain (λ_0) and velocity ($d\lambda_0/dt$) values at t_0. The new strain values are then calculated by solving the finite deformation equations in step 2 for t_1 using T_1. In step 3 the new active tension (T_2) is calculated. $T_2 < T_1$ as $d\lambda/dt_1 < 0$, hence when the new strain is calculated (λ_2) it is greater than λ_1. If the slope of the active tension curve is greater than that of the passive stiffness curve then $\lambda_2 > \lambda_0$ and the solution will not converge,
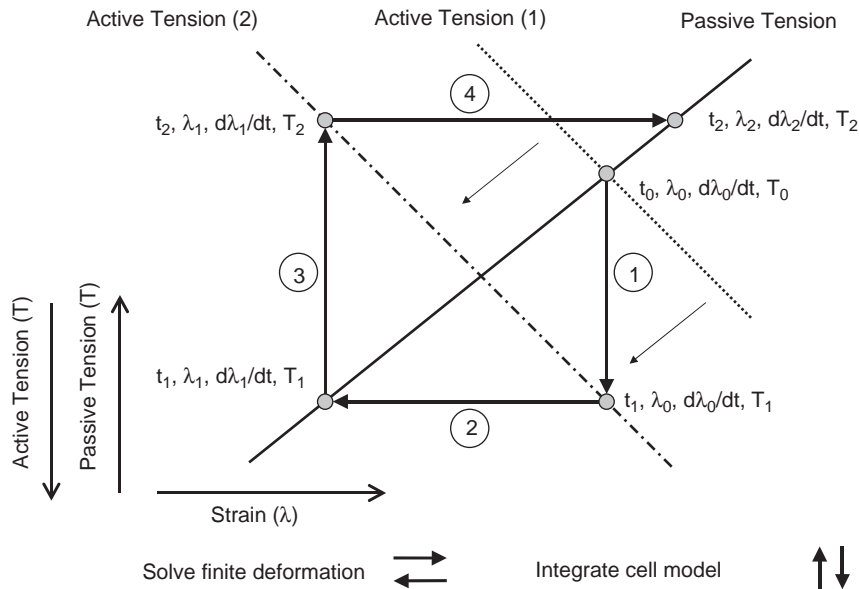

Fig. 3. Schematic diagram showing how the *fixed* coupling method causes velocity dependent instabilities. t_i, λ_i, $d\lambda_i/dt$ and T_i correspond to the time, strain, strain rate and active tension at the ith step. The solid black line is the passive tension and the dashed and dash-dotted line correspond to a low and high level of tension activation. The vertical and horizontal arrows correspond to integrating the cell model through one step and solving the finite deformation equations, respectively. Each of the solve steps is numbered from 1 to 4. The negative of T_a is plotted because strain can be calculated by solving $T_p = -T_a$.

regardless of the time steps taken. In the case of the *update* method step 1 is the same, but in step 2 the solution converges directly to the actual solution at the intersection of T_p and T_a (state 2) curves, as T_a is updated at each intermediate Newton iteration.

To analyse the stability of the velocity dependence of contraction let us again consider a one-dimensional fibre model with no external loads or imposed boundary conditions, bringing us again to $-T_a = T_p$. In this case, we shall consider the muscle to be at a reference length λ_{ref} and that there is a small increase in T_a causing an infinitesimally small decrease in length $\Delta\lambda$ over a period of time Δt, allowing us to assume that λ remains constant to a zero order approximation. Again T_a is calculated within a cell model, but with velocity dependence, using λ and $d\lambda/dt$ from the previous times step. At each iteration between the cell model and the mechanics model the absolute change in length must decrease for convergence (Eq. (11)) due to the monotonic tension length and velocity relationships for both active and passive tension:

$$|\Delta\lambda_{i+1}| < |\Delta\lambda_i|. \tag{11}$$

At each iteration $\Delta\lambda_{i+1}$ is calculated by solving:

$$-\Delta\lambda_{i+1}\frac{dT_p}{d\lambda}\bigg|_{\lambda_i} = \Delta t \frac{dT_a}{dt}(\dot{\lambda}_i), \tag{12}$$

where $dT_p/d\lambda$ can be assumed constant and $(dT_a/dt)(\dot{\lambda})$ is independent of strain since λ remains approximately constant. Applying the requirement for convergence gives:

$$\left|\Delta\lambda_i\frac{dT_p}{d\lambda}\bigg|_{\lambda_i}\right| > \left|\Delta t \frac{dT_a}{dt}(\dot{\lambda}_i)\right|. \tag{13}$$

This can be viewed graphically in Fig. 3 whereby failure to meet the convergence criteria results in an outward spiral of intermediate solutions, causing the solve to fail.

Having identified the sources of instability we quantify the errors and rectify these errors using the *update* coupling method outlined above, applied to a set of our own recently published models. We then compare solution results from the *update* method with an ODE formulation of deformation, whereby length, tension, velocity are updated on the same scale as the other cell state variables, to demonstrate the accuracy of the method. Then we determine the convergence criteria for a simple three-dimensional, transversely isotropic tightly coupled electromechanics problem using the *update* method. Finally, we show that the methods described here are applicable in tissue simulations containing complex inhomogeneous fibre structures following asymmetrical stimulation.

5. Quantifying and rectifying instabilities

To explicitly outline the improved strong coupling method and to link to our results we have used an implementation based on our own recently developed cell models. In our simulations, we have embedded the Niederer et al. (2006) model of active contraction (NHS) in the Niederer and Smith (2007) electrophysiology model (NS) within a spatial representation which has passive constitutive properties governed by the Pole Zero (PZ) constitutive law (Nash and Hunter, 2000). We analyse the length and velocity instabilities and the accuracy of the *update* method using a one-dimensional fibre model, under no external loads and uniform activation or equivalently a zero-dimensional single cell model. Under these assumptions, deformation can be described by a single strain variable (λ) allowing for the analytic calculation of upper bounds on tension activation for the maintenance of stability using the *fixed* coupling method. In the one-dimensional fibre model, strain can be calculated using a system of ODEs (as described in the Appendix), which allows the *update* coupling method to be compared with a solution where strain, strain rate and tension are all updated on the same time scale. The derivation of the ODE representation of deformation and a brief overview of the NHS mechanics component of the NS model and the PZ constitutive law are provided in the Appendix.

5.1. Length dependent instability analysis

In Eq. (10) we derived an upper bound of activation that will lead to a stable solution using the *fixed* coupling method. In the case of NHS coupled to the PZ constitutive law, $\lambda_c = 1 - 1/\beta_0 \approx 0.8$, $T_p(\lambda_c) = -4.94\,\text{kPa}$ and $T_{\text{ref}} = 56.2\,\text{kPa}$, corresponding to a maximum stable activation level of $\hat{z} = 8.79\%$. This is considerably less than expected in any physiological simulation. The problem can be effectively addressed, as outlined above, by using the *update* coupling method, by moving the filament overlap component of T_a into the deformation solve. This is achieved by calculating tension in the cell model using the strain from the previous time step and passing an activation variable ($\hat{T}$), where $\hat{T} = T_{\text{ref}}\hat{z}$, from the cell model to the constitutive relationship, instead of T_a. T_a is then calculated within constitutive law by multiplying $\hat{T}$ by the filament overlap scalar. This gives a new definition of the constitutive relationship (Eq. (14)), which is expressed generally in Eq. (6) and defined specifically for the length dependence in Eq. (7):

$$T^{\text{MN}} = \frac{1}{2}\left(\frac{\partial W}{\partial E_{\text{MN}}} + \frac{\partial W}{\partial E_{\text{NM}}}\right) - pC^{\text{MN}} + \hat{T}(1 + \beta_0(\lambda_i - 1))C^{\text{MN}}. \tag{14}$$

5.2. Velocity dependent instability analysis

The *fixed* coupling method stability is also constrained by Eq. (13) due to velocity dependent instabilities. In the Appendix, we apply Eq. (13) to the NHS model coupled to the PZ constitutive law, resulting in Eq. (15):

$$\left|\frac{\Delta\lambda_i}{\Delta t}\frac{\mathrm{d}T_p}{\mathrm{d}\lambda}\bigg|_{\lambda_i}\right| > \left|T_{\text{ref}}\frac{z}{z_{\text{Max}}}\frac{\mathrm{d}\lambda_i}{\mathrm{d}t}\left((a+1)\sum_{i=1}^{3}A_i + \beta_0\right)\right|, \tag{15}$$

where a corresponds to the curvature of the force velocity relationship, A_i are the weighting coefficients of the components of the fading memory model (defined in Eq. (17)), z is the fraction of available actin sites and z_{Max} is the maximum fraction of available actin sites at a given length. Manipulating Eq. (15) further gives the upper bound of velocity dependent normalized activation (Eq. (16)). This provides an estimate of the upper bound of tension activation in general tissue simulations:

$$\frac{\mathrm{d}T_p}{\mathrm{d}\lambda}\frac{1}{T_{\text{ref}}(\beta_0 + (a+1)\sum_{i=1}^{3}A_i)} > \frac{z}{z_{\text{Max}}}. \tag{16}$$

Eq. (16) states that T_a stiffness must be less than the passive stiffness. The maximum activation that will not generate instabilities for $\lambda \in [0.8, 1.2]$ is only 1.1% of z_{Max}.

In the NHS model $T_a = K(Q_i)T_{\text{ref}}\alpha(z/z_{\text{Max}})$, where K is a nonlinear function (defined in the Appendix by Eq. (26)) of the velocity dependent components of the fading memory model (Q_i). Q_i is defined by

$$\frac{\mathrm{d}Q_i}{\mathrm{d}t} = A_i\frac{\mathrm{d}\lambda}{\mathrm{d}t} - \alpha_i Q_i, \tag{17}$$

where α_i are the exponential rate constants and $i = 1, 2, 3$. To account for this velocity dependence in the deformation solve requires a more temporary assumption that velocity is constant between solves. This allows for the analytic solution of Eq. (17) as a function of the extension ratio:

$$Q_j^{i+1} = \frac{\lambda_{i+1} - \lambda_i}{\Delta t}\frac{A_j}{\alpha_j}(1 - e^{-\alpha_j\Delta t}) + e^{-\alpha_1\Delta t}Q_j^i, \tag{18}$$

where j is the Q index, i is the time step index and Δt is the time between deformation solves. K can then be calculated within the deformation solve at each Newton iteration. The length and velocity dependent tension is still calculated within the cell model for the calculation of tension dependent Ca^{2+} binding to Troponin C (Appendix Eq. (21)). However, the cell model now passes the overlap and velocity independent tension ($\hat{T} = T_{\text{ref}}(z/z_{\text{max}})$) to the mechanics solution which then accounts for the velocity and overlap dependence independently of the cell model. The constitutive equation can

then be written as

$$T^{\mathrm{MN}} = \frac{1}{2}\left(\frac{\partial W}{\partial E_{\mathrm{MN}}} + \frac{\partial W}{\partial E_{\mathrm{NM}}}\right) - pC^{\mathrm{MN}} + \hat{T}K(Q_i)(1 + \beta_0(\lambda_i - 1))C^{\mathrm{MN}}. \tag{19}$$

Although Eq. (19) does not look significantly different from Eq. (6) the modifications importantly produce stable solutions of coupled problems. This formulation eliminates instabilities that occur regardless of the time step between mechanics solutions, thus allowing stable solutions to be calculated within a significantly wider parameter space without any *ad hoc* assumptions about the length or velocity dependent tension at limiting strains. This is now demonstrated below.

6. Simulation results

Three sets of simulations were performed to test the *update* coupling method. The first simulations provide an estimate of the error introduced by solving the mechanics problem and cell model on two different time scales. The second simulations analyse the convergence of a simple three-dimensional test problem. The norms of the errors are provided to allow comparisons with future coupling methods. Furthermore, the convergence test demonstrates that the coupled model is stable at a range of spatial and temporal discretizations. The final simulation shows that the *update* coupling method is stable in complex problems with attributes similar to those expected in a whole heart model.

6.1. Single cell simulations

The error introduced by solving the mechanics and cell model on two different time scales was estimated by comparing strains calculated using the *update* coupling method with the strains calculated using an ODE representation of deformation within a single cell, where λ, $\dot{\lambda}$, T_{a} and T_{p} are updated on the same temporal scale. All ODE model components were solved using the MATLAB ode15s adaptive stepping stiff equation integrator with all options set to default. In the ODE representation λ is added to y in Eq. (2) and $\mathrm{d}\lambda/\mathrm{d}t$ is calculated by differentiating Eq. (34) in the Appendix and rearranging to give $\mathrm{d}\lambda/\mathrm{d}t$ (see Appendix Eq. (41)). We compare the *update* method and the ODE deformation method for single beats using a full electrophysiology cell model (Niederer and Smith, 2007) coupled to a T_{p} constitutive law (Nash and Hunter, 2000) to allow the simulation of feedback of changes in Ca^{2+} buffering on the Ca^{2+} transient. The cell model initial conditions are given in Table 1. Again we solve deformation in the one-dimensional fibre model described in the Appendix.

Fig. 4A plots the tension and strain transients for the model using an ODE to calculate deformation. The T_{a} generated is relatively small as the simulation is for an isotonic contraction, with no applied load. Fig. 4B plots the L2 norm and infinite norm of the difference between the ODE model and the *update* coupling method calculation of λ over the 1000 ms time interval. The L2 norm plateaus at 0.015 between Δt of 2 and 5 ms. The infinite norm also plateaus (at ≈ 0.002) and gives the maximum error, which is $\approx 1.5\%$ of the maximum change in λ (≈ 0.12) during the contraction.

6.2. Isometric contraction simulations

To test the solution accuracy and stability in three-dimensions at different temporal and spatial discretizations we performed a convergence analysis on a rod during isometric contraction. The rod was stimulated from the near end ($x = 0\,\mathrm{mm}$) and the electrical activation propagated rapidly along the length of the rod. This in turn generates a wave of T_{a} that also propagates along the rod. An isometric contraction was chosen to test the convergence as it has unambiguous boundary conditions and the nature of the problem causes a discontinuity in strains where activated tissue is contracting next to elongating inactivated tissue. It was hoped that this would highlight any instabilities.

The rod had dimensions 1, 1 and 8 mm (approximately the same as a rat papillary muscle, Loiselle, 1982) in the z, y and x directions, respectively. The NS cell model was solved on a grid embedded in the finite element mesh which was used to define both the geometry and the solution domain for the finite deformation

Table 1
NS (Niederer and Smith, 2007) initial conditions for zero-dimensional isotonic simulations

Variable	Value	Units
r	0.0022	
s	0.9017	
s_{slow}	0.4613	
Q_1	0	
Q_2	0	
Q_3	0	
y	0.0032	
$[Cl^-]_i$	16.1909	mM
$[CO_2]_i$	1.2361	mM
$[HCO_3^-]_i$	15.1623	mM
$[K^+]_i$	141.6762	mM
$[Na^+]_i$	11.3335	mM
pH_i	7.2096	
$[Ca^{2+}]_i$	7.062×10^{-5}	mM
$[Ca^{2+}]_{SR}$	0.6893	mM
TRPN	0.0676	mM
V	-80.4368	mV
h	0.6713	
j	0.6708	
m	0.0043	
r_{ss}	0.0029	
s_{ss}	0.3023	
z	0.0144	
z_1	0.9896	
z_2	0.0085	
z_3	0.0019	
λ	0.9663	

equations (with a maximum 0.2 mm discretization). The passive material properties were described by a transversely isotropic PZ constitutive law, using the parameters listed in Table 2. The rod geometry was defined by a $2 \times 2 \times n$ tricubic Hermite mesh, where n was increased with the spatial discretization in the x direction. The muscle fibres run along the length of the rod in the x direction. Simulations were performed under conditions of isometric contraction with both ends of the rod constrained by boundary conditions to be in plane. The rod had a conductivity of 0.263, 0.0263 and 0.0263 mS mm^{-1} in the fibre, sheet and normal directions, respectively (Nickerson et al., 2005). The rod was stimulated by 100 µA mm^{-3} current injection for 5 ms at $x = 0$ mm across the whole face. Fig. 5A shows the rod with four elements in the x direction, giving $\Delta x = 2$ mm, at 120 ms after initial activation. The red and blue cones represent the principal strains in tension and compression, respectively. Fig. 5 shows how during the contraction the two ends of the muscle are moving in opposite directions as the wave of tension activation propagates along the rod.

Due to the complexity of even a simple coupled mechanics simulation, no analytic solution is available. Hence the error is calculated by comparing simulation results with simulations results at a high temporal and spatial refinement ($\Delta t = 0.5$ ms and $\Delta x = 0.4$ mm). We calculated the L2 norm of the error in fibre strain at points spaced at 0, 2, 4, 6 and 8 mm along the centre of the rod. We also calculated the Normalized Integral of the Difference between the highly refined numerical solution and the current numerical solution Squared (NIDS) (Eq. (20)) along the centre of the rod:

$$\text{NIDS error} = \sqrt{\frac{\int(\lambda|_{\Delta x=0.4\,\text{mm}\ \Delta t=0.5\,\text{ms}} - \lambda_{\text{numerical}})^2\,\mathrm{d}x}{\int \lambda|_{\Delta x=0.4\,\text{mm}\ \Delta t=0.5\,\text{ms}}\,\mathrm{d}x}}. \tag{20}$$

Both measures of error were calculated for mechanics time steps (Δt) of 0.5, 1, 2 and 5 ms and spatial discretization along the length of the rod (Δx) of 8, 4, 2, 1 and 0.4 mm, corresponding to 366, 591, 1041, 1941
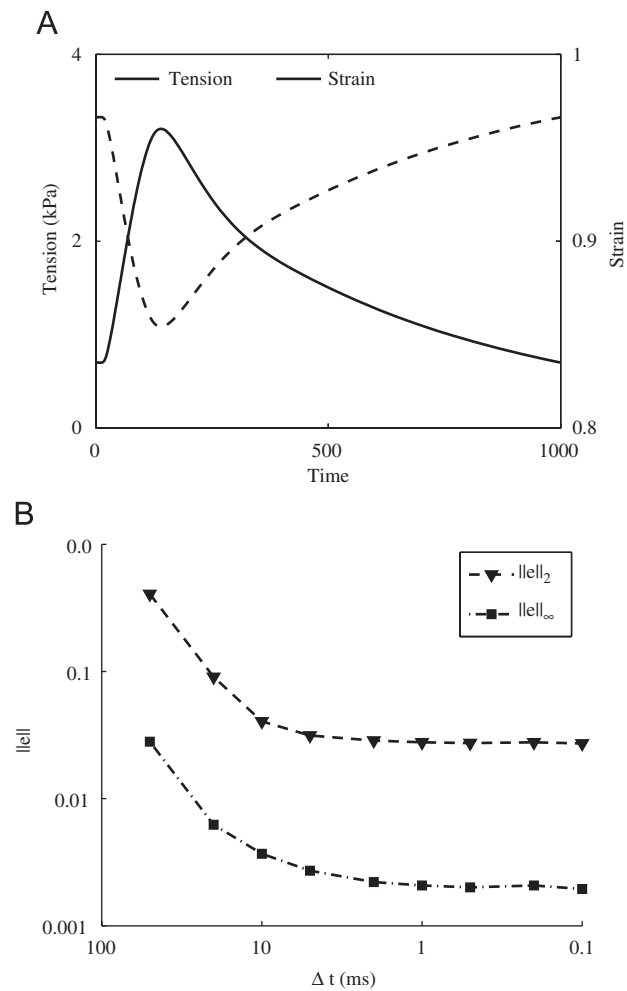
A

B

Fig. 4. (A) Plot of the strain (dashed line) and tension (solid line) calculated using the ODE representation of deformation and the NS and PZ models. (B) L2 and infinite norms of the difference between the *update* and ODE deformation representation of the coupled NS and PZ model for different time steps (Δt) between the calculations of converged mechanics solutions in the *update* coupling method.

Table 2
Pole Zero (Nickerson et al., 2005) model parameters

Parameter	Value	Units
a_1	0.475	
a_2, a_3	0.619	
a_4, a_5, a_6	0.8	
k_1	2.22	kPa
k_2, k_3	2.22	kPa
k_4, k_5, k_6	1.0	kPa
b_1	1.5	
b_2, b_3	1.5	
b_4, b_5, b_6	1.2	

and 4695 degrees of freedom (DOF), respectively. Fig. 5B plots the strain at the five points with $\Delta t = 0.5$ ms and $\Delta x = 0.4$ mm. The curves are all smooth and show no oscillations.

Fig. 5C–G plots the L2 norms for each of the strains recorded at the five points along the rod. At points $x = 0$, 4 and 8 mm the errors decrease as the model is refined spatially. In the case of the error at $x = 2$ and
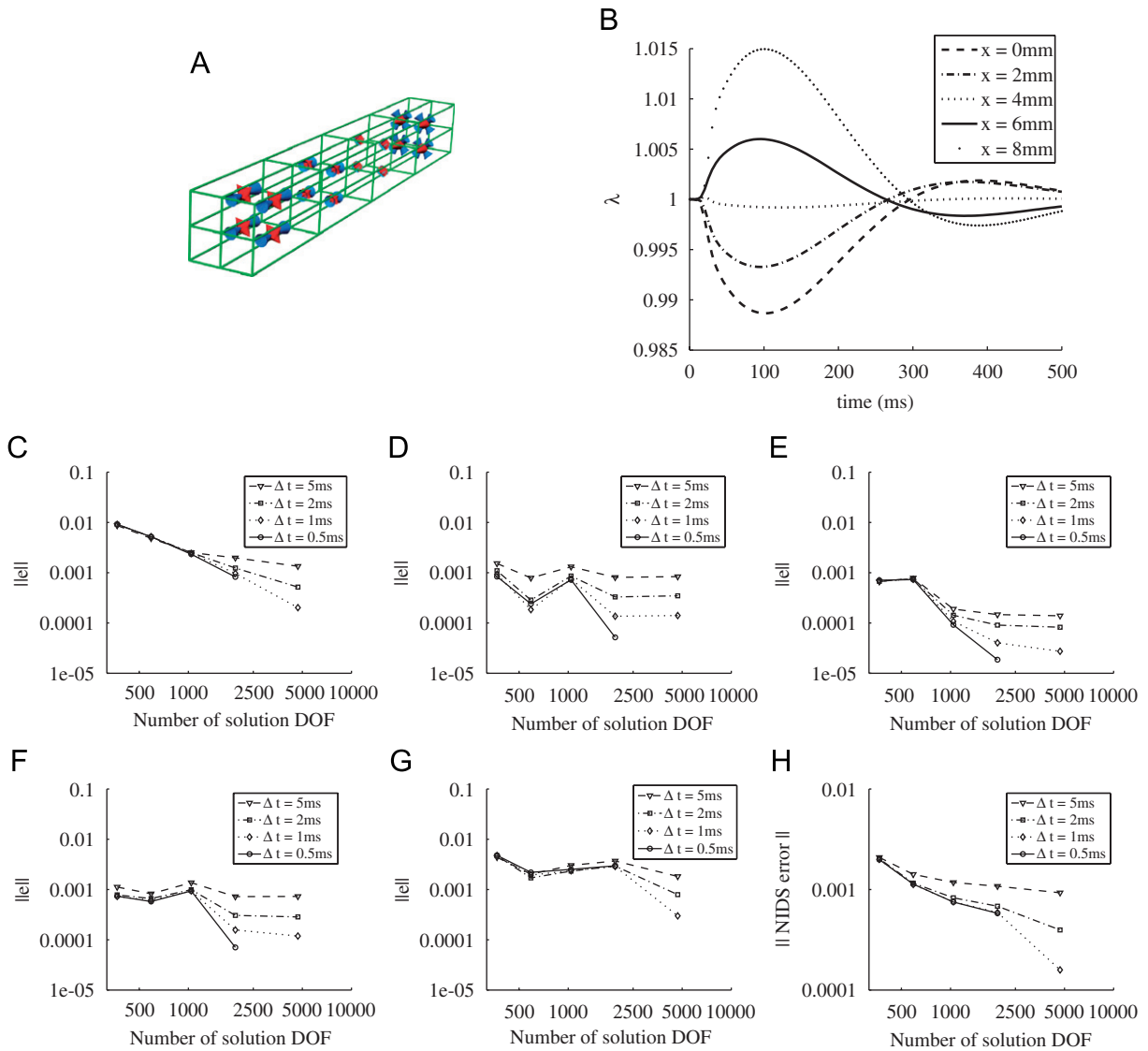
Fig. 5. (A) The rod mesh and principal strains at 120 ms after activation. The orientation and magnitude of the cones indicates the direction and magnitude of the principal strains with red indicating tension and blue compression. (B) Fibre strain transients at 0, 2, 4, 6 and 8 mm along the centre of the rod. (C)–(G) the L2 norm of the difference between the current numerical solution and the highly refined numerical solution at 0, 2, 4, 6 and 8 mm along the centre of the rod, respectively. (H) The NIDS error along the central axis of the rod.

6 mm the error is relatively small compared to $x = 0$ and 8 mm and does not change with spatial refinement. Temporal refinement appears to have only nominal effects in coarse meshes and only starts to affect the error after $\Delta x < 4$ mm.

As the NIDS error is a ratio, it can be interpreted as a percentage error over the domain. The NIDS error was calculated at each time step and then the L2 norm of the NIDS error was calculated and plotted in Fig. 5H. The L2 norm of the NIDS error is less than 0.1% for $\Delta x \leqslant 4$ mm and $\Delta t < 5$ ms. The error also decreases monotonically as Δx decreases for all Δt values. As Δt decrease the NIDS error plateaus leading to the error for $\Delta t = 0.5$ ms and $\Delta t = 1$ ms to be approximately equal, at all levels of mesh refinement. Both the point and NIDS measures of error show that the solution is converging, confirming that the solution is stable.

6.3. Inhomogeneous and asymmetric simulations

To demonstrate the stability of the *update* coupling method in complex geometries we performed simulations in a cube with dimensions $2 \times 2 \times 2$ mm with an inhomogeneous fibre field and asymmetrical activation. The cube was described by a $2 \times 2 \times 2$ tricubic Hermite mesh. The fibre and imbrication angles varied linearly across the cube from $-60°$ to $60°$ and $-5°$ to $5°$, respectively, as shown by the arrow sheets in Fig. 6A, similar to the fibre orientations observed across the left ventricle wall. Again an NS cell model was used with a PZ constitutive law. The cell model was stimulated by $100 \, \mu A \, mm^{-3}$ current injection for 5 ms at a group of cells within a 0.5 mm radius of the corner indicated by the red sphere in Fig. 6A. The propagation of the activation wave is asymmetrical as demonstrated by the iso-planes, moving from red to blue with time, showing the location of 0 mV at 2, 4, 6 and 8 ms after the initial stimulation. The bottom face of the cube was held flat and fixed in plane as indicated by the grey surface in Fig. 6A. The finite deformation equations were solved every 1 ms, using the *update* coupling method. Fig. 6B–I shows the cube deformation at 0, 50, 100, 150,
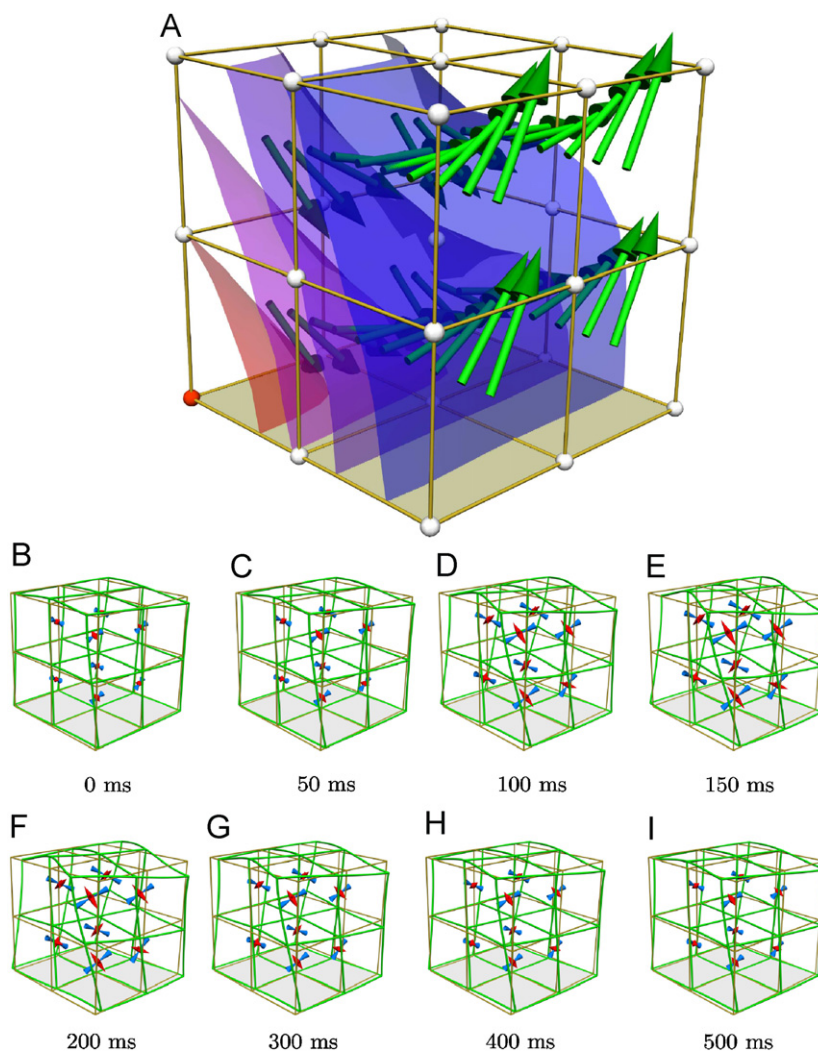

Fig. 6. (A) The cube mesh with green arrows indicating fibre direction. The red node indicates the source of the stimulus current. The four isoplanes changing from red to blue with time, indicate the position of 0 mV at 2, 4, 6 and 8 ms. The grey panel indicates the surface constrained by boundary conditions to be in plane during the simulations. (B)–(I) show the deformed (green) and undeformed (gold) meshes. The orientation and magnitude of the cones indicates the direction and magnitude of the principal strains with red indicating tension and blue compression.

200, 300, 400 and 500 ms. Again the red and blue cones correspond to tension and compression, respectively. The green and gold meshes show the deformed and undeformed meshes, respectively.

The initial deformed mesh (green mesh Fig. 6B) is not the same as the undeformed mesh (gold mesh Fig. 6B) as the small tensions generated by the cell at rest cause the tissue to distort even in the resting state. As the cube is activated the fibres pull in opposite directions causing the cube to twist into a highly deformed state. However, the coupling between the activation and deformation remains stable.

7. Discussion

In this study, we have identified sources of instabilities in the *fixed* strong coupling method. We have proposed a new *update* strong coupling method that addresses these instabilities. We have shown that solving the mechanics problem and cell model on two different time scales induces nominal levels of error in zero-dimensional simulations. We have performed temporal and spatial convergence analysis for isometric contractions in a simple geometry. Finally, we have shown that the coupling method produces stable solutions in a model containing many of the complexities present in the heart.

The *fixed* strong coupling method induced instabilities in the coupled NS and PZ model. The significance of both the length and velocity dependent instabilities are invariably dependent on the model parameters. The length dependence is very sensitive to the slope of the maximum isometric tension length curve (β_0). Arguably, this value should be similar for all species and temperature consistent models but the use of disparate experimental data sets leads to significantly different values. However, even in the absence of regions of strain where α is undefined or causes negative tension values, the inclusion of the filament overlap effects in the PZ definition allows for the Newton iteration to converge to the correct solution in a single solution of the finite deformation equations without iterating between the mechanics solution and the cell model.

The velocity dependent instability criterion states that the slope of the T_p curve (passive stiffness) must be greater than the slope of the T_a curve (active tension stiffness) (Eq. (13)), analogous to the restitution hypothesis used analyse the stability of wave propagation in cardiac electrophysiology (Garfinkel et al., 2000). The NHS formulation is fit using dynamic stiffness data and hence an analytic definition of the active tension stiffness is available. Generally models of active contraction are not fit to dynamic stiffness data (Rice et al., 2003; Huxley, 1957; Sachse et al., 2003; Taber et al., 1996; Peterson and Alpert, 1991), in these cases the T_a stiffness can be calculated by simulating the change in tension following an instantaneous small change in strain. The change in tension over the change in strain then provides an approximate measure of the T_a stiffness. Incorporating the velocity dependence into the finite deformation equations may prove more challenging for different implementations of velocity dependencies, however, two alternate solutions exist. Firstly, biophysical multi-state cross bridge models (Rice et al., 2003; Huxley, 1957; Sachse et al., 2003; Peterson and Alpert, 1991) can be converted to the fading memory formulation as described by Smith et al. (2003) and the techniques described above can be applied to achieve numerical stability. Alternately, in the case of phenomenological models (Taber et al., 1996), the relevant components of the cell model can be integrated within the deformation solve. Although potentially computationally intensive, the relevant cell model components will only need to be solved at the Gauss points where the constitutive equation (Eq. (6)) is evaluated (Nickerson et al., 2005). This is likely to be a significantly coarser grid than the cell model solution grid and as such prove to be significantly more tractable than resolving the coupled cell model on the high resolution electrophysiology grid.

The zero-dimensional model quantifies the error introduced by solving the mechanics problem and cell model on two different time scales. Although the method is stable, with both the L2 norm and infinite norm converging to a plateau, it does introduce errors. The level of error introduced is small at $\approx 1.5\%$ and noncumulative. However, the error is not reduced upon further temporal refinement, which is undesirable. We suspect the source of this error is that the tension activation level and the T_a dependent Ca^{2+} binding to TnC are calculated using the λ and $d\lambda/dt$ values from the previous time step. The size of the error introduced by updating length at discrete time intervals does not imply that the length and tension dependent components absent from the *update* method are not significant in coupled electromechanics simulations. However, it does suggest that the effects of the absent components occur over time scales larger than the time period between

calculating successive mechanics solution and hence do not affect the stability of coupled electromechanics solution.

The isometric contraction simulations results, to our knowledge, represent the first convergence analysis of a tissue model of strongly coupled excitation and contraction. As such they provided a comparison for future studies and provide a useful resource in themselves. Furthermore, the simulations demonstrated that the coupling method was capable of producing stable and converged solutions. The L2 norm was $\approx 10^{-3}$–10^{-4} for the more refined combinations of Δx and Δt (see Fig. 5C–G). Notably, the error at the external nodes was considerably higher than the internal nodes. Fortunately, in the ventricle the base is the only boundary with near perpendicular fibres, hence a coarser mesh may be sufficient to achieve converged solutions over the majority of a ventricle model. The NIDS error, plotted in Fig. 5H, was small ($\approx 0.1\%$) for $\Delta t < 5$ ms and $\Delta x \leqslant 4$ mm. The NIDS error also decreased monotonically for all temporal and spatial refinements, indicating that as a whole the solution was stable and converging. The degree of refinement required is determined by the desired level of accuracy and computational resources. To achieve a level of error within the tolerance of previous modeling studies of 10^{-3} (Nash and Hunter, 2000) would require a Δx value of $1-2$ mm and a Δt value of $1-2$ ms.

Extending the *update* coupling method to anatomical or even simplified heart geometries is beyond the scope of this paper. However, to demonstrate the capacity of the method to provide stable solutions in simulations containing many of the challenging attributes present in heart simulations, we have performed a simulation in a three-dimensional cube with asymmetric activation and a transversely isotropic fibre field with variation in both the fibre and imbrication angles. This simulation demonstrates how the coupling method is stable even under large and complex deformations. Hence the *update* coupling method appears likely to be a useful tool in solving tightly coupled electromechanics solutions in whole heart simulations.

There are no standard tests for the quality of a coupled electromechanics solution and the majority of coupled mechanics papers do not show any convergence testing (Kerckhoffs et al., 2005; Nickerson et al., 2005; Smith et al., 2003; Nash and Hunter, 2000). The zero-dimensional model and the isometric contraction model have simple boundary and initial conditions and in the case of the isometric contraction model simple geometry. The zero-dimensional model in particular can be described as a system of ODEs and is readily implemented (as opposed to the necessary finite deformation and bi/mono domain code required for the isometric contraction model). These attributes lend these models towards being used as standard tests to validate and compare future coupling methods.

In this study, we have developed a new numerical method to account for an important physiological phenomenon. The method developed is both accurate and stable. This has led to a significant improvement in the computational tractability of excitation–contraction simulations in the heart. In the future the *update* method will hopefully contribute to developing a strongly coupled, biophysically based, integrated heart model.

Acknowledgements

Appendix A

A.1. Overview of NHS and PZ models

The NHS contraction model has $[Ca^{2+}]_i$, strain (λ) and velocity ($\dot{\lambda}$) as its three input variables, which are used to calculate T_a. The model parameters are given in Table A1. $[Ca^{2+}]_i$ is provided by the NS

Table A1
NHS (Niederer et al., 2006) model parameters

Parameter	Value	Units
k_{on}	100	$mM^{-1}\,ms^{-1}$
k_{off}	0.2	ms^{-1}
β_0	4.9	
β_1	-4.0	
Ca_{50ref}	0.00105	mM
$[Ca^{2+}]_{TRPNMax}$	0.07	mM
γ_{trpn}	2.0	
α_0	0.008	ms^{-1}
α_{r1}	0.002	ms^{-1}
α_{r2}	0.0017	ms^{-1}
n_{Hill}	3.0	
K_z	0.15	
n_{Rel}	3	
A_1	-29	
A_2	138	
A_3	129	
α_1	0.03	ms^{-1}
α_2	0.13	ms^{-1}
α_3	0.625	ms^{-1}
a	0.35	
z_p	0.85	
T_{ref}	56.2	kPa

electrophysiology model and the strain and strain rate are provided by the mechanics solution. The NHS model begins with the concentration of Ca^{2+} bound to TnC, which is calculated using:

$$\frac{d[Ca^{2+}]_{TRPN}}{dt} = k_{on}[Ca^{2+}]_i([Ca^{2+}]_{TRPNMax} - [Ca^{2+}]_{TRPN}) - k_{off}\left(1 - \frac{T}{\gamma_{trpn}T_{ref}}\right)[Ca^{2+}]_{TRPN}, \quad (21)$$

where $[Ca^{2+}]_i$ is the cytosolic Ca^{2+}, $[Ca^{2+}]_{TRPN}$ is the concentration of Ca^{2+} bound to the low affinity binding sites on Troponin C (TnC), k_{off} is the disassociation rate, k_{on} is the association rate, γ_{trpn} is the tension dependence, T_{ref} is a reference tension and $[Ca^{2+}]_{TRPNMax}$ is the maximum concentration of Ca^{2+} that can bind to TnC. The fraction of actin sites available is defined by Eqs. (22)–(24).

$$Ca_{50} = Ca_{50ref}(1 + \beta_1(\lambda - 1)), \quad (22)$$

$$Ca_{TRPN_{50}} = [Ca^{2+}]_{TRPNMax}\frac{Ca_{50}}{Ca_{50} + k_{off}/k_{on}(1 - (1 + \beta_0(\lambda - 1))1/2\gamma_{trpn})}, \quad (23)$$

$$\frac{dz}{dt} = \alpha_0\left(\frac{[Ca^{2+}]_{TRPN}}{Ca_{TRPN_{50}}}\right)^{n_{Hill}}(1 - z) - \alpha_{r1}z - \alpha_{r2}\frac{z^{n_{Rel}}}{z^{n_{Rel}} + K_z^{n_{Rel}}}, \quad (24)$$

where z is the fraction of available actin sites, α_0 is the rate of activation, α_{r1} and α_{r2} are the rates of relaxation, Ca_{50}, Ca_{50ref} and $Ca_{TRPN_{50}}$ are the $[Ca^{2+}]_i$, $[Ca^{2+}]_i$ reference and the Ca^{2+} bound to TnC half activation concentrations, respectively, β_0 and β_1 are the tension and half activation length dependence coefficients and n_{Hill} and n_{Rel} are the nonlinear activation and relaxation coefficients. The velocity dependence is accounted for by the fading memory model (28):

$$\frac{dQ_i}{dt} = A_i\frac{d\lambda}{dt} - \alpha_iQ_i, \quad (25)$$

$$K = \begin{cases} \dfrac{a\sum_{i=1}^{3}Q_i + 1}{1 - \sum_{i=1}^{3}Q_i}, & Q \leqslant 0, \\[3mm] \dfrac{1 + (2+a)\sum_{i=1}^{3}Q_i}{1 + \sum_{i=1}^{3}Q_i}, & Q > 0, \end{cases} \tag{26}$$

where α_i are the exponential rate constants and A_i are the associated weighting coefficients, a controls the curvature of the force–velocity curve, Q_i are phenomenological state variables lumping the contribution of the crossbridges to tension and K is the velocity dependence scalar, which represents the ensemble effects. Finally tension is calculated from the product of a filament overlap function (Eq. (27)), the reference tension, the velocity dependence scalar (Eq. (26)) and the normalized fraction of available actin sites (Eq. (29)), giving Eq. (30):

$$\alpha = (1 + \beta_0(\lambda - 1)), \tag{27}$$

$$K_2 = \alpha_{r2}\frac{z_p^{n_{Rel}}}{z_p^{n_{Rel}} + K_z^{n_{Rel}}}\left(1 - n_{Rel}\frac{K_z^{n_{Rel}}}{z_p^{n_{Rel}} + K_z^{n_{Rel}}}\right), \quad K_1 = \alpha_{r2}\frac{z_p^{n_{Rel}-1}n_{Rel}K_z^{n_{Rel}}}{(z_p^{n_{Rel}} + K_z^{n_{Rel}})^2}, \tag{28}$$

$$z_{Max} = \frac{\alpha_0/(Ca_{TRPN_{50}}/[Ca^{2+}]_{TRPNMax})^{n_{Hill}} - K_2}{\alpha_{r1} + K_1 + \alpha_0/(Ca_{TRPN_{50}}/[Ca^{2+}]_{TRPNMax})^{n_{Hill}}}, \tag{29}$$

$$T_a = T_{ref}\alpha K\frac{z}{z_{Max}}, \tag{30}$$

where z_{Max} is the maximum fraction of available actin sites at a given length. T_a is the same as T_a in Eq. (6) and provides the link between tension calculated at the cellular scale and deformation calculated at the tissue spatial scale.

At the tissue spatial scale, as outlined above, mechanics are solved using the finite deformation equations. These equations require the definition of a constitutive law, which describes the relationship between stress and strain in the tissue. In the simulations performed in this study, we apply the PZ constitutive law (Nash and Hunter, 2000). The law is composed of six components describing the stiffness of cardiac tissue with respect to the sheet, fibre and sheet normal microstructure, as given in Eq. (31):

$$\begin{aligned} W = &\, k_1\frac{e_{11}^2}{(a_1 - e_{11})^{b_1}} + k_2\frac{e_{22}^2}{(a_2 - e_{22})^{b_2}} + k_3\frac{e_{33}^2}{(a_3 - e_3)^{b_3}} \\ &+ k_4\frac{e_{12}^2}{(a_4 - e_{12})^{b_4}} + k_5\frac{e_{23}^2}{(a_5 - e_{23})^{b_5}} + k_6\frac{e_{31}^2}{(a_6 - e_{31})^{b_6}}, \end{aligned} \tag{31}$$

where e_{MN} are the components of the Green strain tensor (Eq. (3)) referred to material coordinates aligned with the structurally defined axis of the tissue. In the first coupled tissue example presented in the results we reduce Eq. (31) by modeling a transversely isotropic cylinder with no external loading (approximating a papillary or trabeculae during an isotonic contraction). Under these conditions the passive component of Eq. (6) in the fibre direction (T_p) can be calculated using Eq. (32), taking e_{11} as the fibre direction and $e_{22} = e_{33}$ as the material is transversely isotropic:

$$T_p = k_1\frac{e_{11}}{(a_1 - e_{11})^{b_1}}\left(2 + \frac{b_1 e_{11}}{a_1 - e_{11}}\right) - 2k_2\frac{e_{22}}{(a_2 - e_{22})^{b_2}}\left(2 + b_2\frac{e_{22}}{a_2 - e_{22}}\right). \tag{32}$$

Assuming isovolumetric deformation gives the relationship between fibre strain (λ) and the Green strain components:

$$e_{11} = \frac{1}{2}(\lambda^2 - 1), \quad e_{22} = \frac{1}{2}\left(\frac{1}{\lambda} - 1\right). \tag{33}$$

Resolving Eq. (4) given the simplified geometry and lack of external loads gives Eq. (34):

$$T_p = -T_a \tag{34}$$

allowing λ to be calculated directly by solving this equation, where T_p and T_a are determined from Eqs. (33) and (21) to Eq. (30), respectively.

A.2. Tension and strain derivatives

The derivatives of the active tension and passive tension are required in solving deformation using a system of ODEs in a zero-dimensional model and in finding the upper bound on tension activation for velocity dependent stability. The rate of change of T_a is calculated by differentiating Eq. (30) with respect to time:

$$\frac{dT_a}{dt} = T_{ref}\left(\frac{dK}{dt}\frac{z}{z_{Max}}\alpha + K\frac{z}{z_{Max}}\frac{d\alpha}{dt} + K\frac{dz}{dt}\frac{1}{z_{Max}}\alpha - \frac{1}{z_{max}^2}\frac{dz_{max}}{dt}Kz\alpha\right),\tag{35}$$

where dz/dt is defined by Eq. (24), $d\alpha/dt$ is given by

$$\frac{d\alpha}{d\lambda} = \beta_0,\tag{36}$$

$$\frac{d\alpha}{dt} = \frac{d\alpha}{d\lambda}\frac{d\lambda}{dt},\tag{37}$$

dK/dt is defined by

$$\frac{dK}{dt} = \begin{cases} \dfrac{a+1}{(\sum_{i=1}^{3}Q_i - 1)^2}\left(\sum_{i=1}^{3}A_i\dfrac{d\lambda}{dt} - \sum_{i=1}^{3}\alpha_i Q_i\right), & Q \leqslant 0, \\[4mm] \dfrac{a+1}{(\sum_{i=1}^{3}Q_i + 1)^2}\left(\sum_{i=1}^{3}A_i\dfrac{d\lambda}{dt} - \sum_{i=1}^{3}\alpha_i Q_i\right), & Q > 0 \end{cases}\tag{38}$$

and $-(1/z_{max}^2)\,dz_{max}/dt$ is defined by

$$\kappa_1 = Ca_{50ref}\beta_1 - \frac{1}{2}\frac{k_{off}}{k_{on}}\frac{\beta_0}{\gamma_{trpn}}, \quad \kappa_2 = Ca_{50} + \frac{k_{off}}{k_{on}}\left(1 - \frac{1 + \beta_0(\lambda - 1)}{2\gamma_{trpn}}\right),$$

$$\kappa_3 = n_{Hill}\frac{\alpha_0}{(Ca_{50}/\kappa_2)^{n_{Hill}}}\left(\frac{Ca_{50ref}}{Ca_{50}}\beta_1 - \frac{\kappa_1}{\kappa_2}\right),$$

$$-\frac{1}{z_{max}^2}\frac{dz_{max}}{d\lambda} = \kappa_3\frac{1}{(\alpha_0/(Ca_{50}/\kappa_2)^{n_{Hill}} - K_2)^2}(\alpha_{r1} + K_1 + K_2),$$

$$-\frac{1}{z_{max}^2}\frac{dz_{max}}{dt} = -\frac{1}{z_{max}^2}\frac{dz_{max}}{d\lambda}\frac{d\lambda}{dt},\tag{39}$$

where K_1 and K_2 are defined in Eq. (28).

The rate of change of passive tension is given by the product of passive stiffness and the strain rate $(dT_p/dt = (dT_p/d\lambda)d\lambda/dt)$. Passive stiffness is calculated by differentiating Eq. (32), giving

$$\frac{dT_p}{d\lambda} = k_1\lambda\frac{1}{(a_1 - e_{11})^{b_1}}\left(2 + b_1\frac{e_{11}}{a_1 - e_{11}}\left(4 + (b_1 + 1)\frac{e_{11}}{a_1 - e_{11}}\right)\right)$$

$$+ k_2\frac{1}{\lambda^2}\frac{1}{(a_2 - e_{22})^{b_2}}\left(2 + b_2\frac{e_{22}}{a_2 - e_{22}}\left(4 + (b_2 + 1)\frac{e_{22}}{a_2 - e_{22}}\right)\right).\tag{40}$$

The strain rate can then be calculated by substituting $C^{MN} = 1/\lambda^2$ into Eq. (6) and differentiating with respect to time then substituting in Eqs. (40) and (35) and rearranging to give:

$$\frac{d\lambda}{dt} = -\frac{T_{ref}/\lambda^2((dz/dt)(1/z_{Max})\alpha K + (z/z_{Max})\alpha(a + 1/(\sum_{i=1}^{3} Q_i \pm 1)^2)\sum_{i=1}^{3}\alpha_i Q_i)}{(dT_p/d\lambda)1/T_{ref} - (1/z_{max}^2)(dz_{max}/d\lambda)Kz\alpha + (d\alpha/d\lambda)K(z/z_{Max}) + (z/z_{Max})\alpha(a + 1/(\sum_{i=1}^{3} Q_i \pm 1)^2)\sum_{i=1}^{3}A_i - (2/\lambda^3)T_a},$$

(41)

where the $\pm$ signs indicate the difference piecewise components of dK/dt defined in Eq. (38).

A.3. Velocity dependent instability analysis

The general *fixed* coupling method velocity dependent constraint (Eq. (13)) was derived above. In the specific case of the NHS model coupled to the PZ model $dT_p/d\lambda$ and dT_a/dt from Eq. (13) are defined above by Eqs. (40) and (35), respectively. Assuming the model is at rest in a steady state, such that $\lambda = 1$, $Q_i = 0$ and $dz/dt = 0$ and given that $-(1/z_{Max}^2)dZ_{Max}/dt \ll dK/dt + d\alpha/dt$, $K|_{Q_i=0} = 1$ and $\alpha|_{\lambda=1} = 1$, then Eq. (35) reduces to

$$\frac{dT_a}{dt} = T_{ref}\frac{z}{z_{Max}}\left(\frac{dK}{dt} + \frac{d\alpha}{dt}\right),$$

(42)

where $d\alpha/dt$ is defined by Eq. (37). dK/dt is defined by Eq. (38) and reduces to Eq. (43), given the assumptions noted above:

$$\left.\frac{dK}{dt}\right|_{Q_i=0, i=1,2,3} = \frac{d\lambda}{dt}(a + 1)\sum_{i=1}^{3}A_i.$$

(43)

Combining Eqs. (42), (37), (43) and (13) gives:

$$\left|\frac{\Delta\lambda_i}{\Delta t}\frac{dT_p}{d\lambda}\right| > \left|T_{ref}\frac{z}{z_{Max}}\frac{d\lambda_i}{dt}\left((a + 1)\sum_{i=1}^{3}A_i + \beta_0\right)\right|.$$

(44)

References

Alvarez, B.V., Perez, N.G., Ennis, I.L., Camilion de Hurtado, M.C., Cingolani, H.E., 1999. Mechanisms underlying the increase in force and Ca^{2+} transient that follow stretch of cardiac muscle: a possible explanation of the anrep effect. Circ. Res. 85, 716–722.

Alvarez, B.V., Fujinaga, J., Casey, J.R., 2001. Molecular basis for angiotensin ii-induced increase of chloride/bicarbonate exchange in the myocardium. Circ. Res. 89, 1246–1253.

Buist, M., Sands, G., Hunter, P., Pullan, A., 2003. A deformable finite element derived finite difference method for cardiac activation problems. Ann. Biomed. Eng. 31, 577–588 (Describes method for collocation for finite element derived finite difference).

Costa, K.D., Hunter, P.J., Rogers, J.M., Guccione, J.M., Waldman, L.K., McCulloch, A.D., 1996. A three dimensional finite element method for large elastic deformations of ventricular myocardium. 1. cylindrical and spherical polar coordinates. J. Biomech. Eng. Trans. ASME 118, 452–463.

Fuchs, F., Wang, Y.P., 1996. Sarcomere length versus interfilament spacing as determinants of cardiac myofilament Ca^{2+} sensitivity and Ca^{2+} binding. J. Mol. Cell. Cardiol. 28, 1375–1383.

Fuchs, F., Whaley, M.E., Hofmann, P.A., 1988. Binding of Ca^{2+} to skinned muscle-fibers at short sarcomere-length—comparison of skeletal and cardiac-muscle. Biophys. J. 53 (Part 2), A566.

Garfinkel, A., Kim, Y.-H., Voroshilovsky, O., Qu, Z., Kil, J.R., Lee, M.-H., Karagueuzian, H.S., Weiss, J.N., Chen, P.-S., 2000. From the cover: preventing ventricular fibrillation by flattening cardiac restitution. Proc. Natl. Acad. Sci. 97, 6061–6066.

Hunter, P.J., McCulloch, A.D., ter Keurs, H., 1998. Modelling the mechanical properties of cardiac muscle. Prog. Biophys. Mol. Biol. 69, 289–331.

Huxley, A.F., 1957. Muscle structure and theories of contraction. Prog. Biophys. Mol. Biol. 7, 255.

Kerckhoffs, R.C.P., Faris, O.P., Bovendeerd, P.H.M., Prinzen, F.W., Smits, K., McVeigh, E.R., Arts, T., 2005. Electromechanics of paced left ventricle simulated by straightforward mathematical model: comparison with experiments. Am. J. Physiol. 289, H1889–H1897.

Kerckhoffs, R.C.P., Healy, S.N., Usyk, T.P., McCulloch, A.D., 2006. Computational methods for cardiac electromechanics. Proc. IEEE 94 769–783, 0018–9219.

Lab, M.J., 1999. Mechanosensitivity as an integrative system in heart: an audit. Prog. Biophys. Mol. Biol. 71, 7–27.

Loiselle, D.S., 1982. Stretch-induced increase in resting metabolism of isolated papillary muscle. Biophys. J. 38, 185–194.

Malvern, L., 1969. Introduction to the Mechanics of a Continuous Medium. Prentice-Hall, Englewood Cliffs, NJ.

Nash, M.P., Hunter, P.J., 2000. Computational mechanics of the heart—from tissue structure to ventricular function. J. Elasticity 61, 113–141.

Nickerson, D., Smith, N., Hunter, P., 2005. New developments in a strongly coupled cardiac electromechanical model. Europace 7, S118–S127.

Niederer, S.A., Smith, N.P., 2007. Modeling the anrep effect in rat ventricular myocytes. Biophys. J. 92 (11), 4030–4044.

Niederer, S.A., Hunter, P.J., Smith, N.P., 2006. A quantitative analysis of cardiac myocyte relaxation: a simulation study. Biophys. J. 90, 1697–1722.

Peterson, J.N., Alpert, N.R., 1991. Time course of mechanical efficiency during afterloaded contractions in isolated cardiac muscle. Am. J. Physiol. 261, 27–29.

Petroff, M.G.V., Kim, S.H., Pepe, S., Dessy, C., Marban, E., Balligand, J.-L., Sollott, S.J., 2001. Endogenous nitric oxide mechanisms mediate the stretch dependence of Ca^{2+} release in cardiomyocytes. Nat. Cell Biol. 3, 867–873.

Plonsey, R., Barr, R.C., 1984. Current flow patterns in two-dimensional anisotropic bisyncytia with normal and extreme conductivities. Biophys. J. 45, 557–571.

Razumova, M.V., Bukatina, A.E., Campbell, K.B., 1999. Stiffness-distortion sarcomere model for muscle simulation. J. Appl. Physiol. 87, 1861–1876.

Rice, J.J., Winslow, R.L., Hunter, W.C., 1999. Comparison of putative cooperative mechanisms in cardiac muscle: length dependence and dynamic responses. Am. J. Physiol. 276, H1734–H1754.

Rice, J.J., Stolovitzky, G., Tu, Y., de Tombe, P.P., 2003. Ising model of cardiac thin filament activation with nearest-neighbor cooperative interactions. Biophys. J. 84, 897–909.

Sachse, F.B., Seemann, G., Chaisaowong, K., Weiss, D., 2003. Quantitative reconstruction of cardiac electromechanics in human myocardium: assembly of electrophysiologic and tension generation models. J. Cardiovasc. Electrophysiol. 14, S210–S218.

Schmid, H., Nash, M.P., Young, A.A., Hunter, P.J., 2006. Myocardial material parameter estimation—a comparative study for simple shear. J. Biomech. Eng. 128, 742–750.

Schmitt, O.H., 1969. Biological information processing using the concept of interpenetrating domains. Information Processing in the Nervous System. Springer, New York.

Sermesant, M., Delingette, H., Ayache, N., 2006. An electromechanical model of the heart for image analysis and simulation. IEEE Trans. Med. Imaging, 25, 612–625, 0278–0062.

Smith, N.P., Buist, M.L., Pullan, A.J., 2003. Altered *t* wave dynamics in a contracting cardiac model. J. Cardiovasc. Electrophysiol. 14 (Suppl. S), S203–S209.

Taber, L.A., Yang, M., Podszus, W.W., 1996. Mechanics of ventricular torsion. J. Biomech. 29, 745–752.

Tomlinson, K., Hunter, P.J., Pullan, A.J., 2002. A finite element method for an eikonal equation model of myocardial excitation wave-front propagation. SIAM J. Appl. Math. 63, 324–350.

Usyk, T.P., McCulloch, A.D., 2003. Relationship between regional shortening and asynchronous electrical activation in a three-dimensional model of ventricular electromechanics. J. Cardiovasc. Electrophysiol. 14, S196–S202.

Vendelin, M., Bovendeerd, P.H.M., Arts, T., Engelbrecht, J., van Campen, D.H., 2000. Cardiac mechanoenergetics replicated by cross-bridge model. Ann. Biomed. Eng. 28, 629–640, doi:10.1114/1.1305910.

Watanabe, H., Sugiura, S., Kafuku, H., Hisada, T., 2004. Multiphysics simulation of left ventricular filling dynamics using fluid-structure interaction finite element method. Biophys. J. 87, 2074–2085.

Yin, F., 1981. Ventricular wall stress. Circ. Res. 49, 829–842.

Zeng, T., Bett, G.C.L., Sachs, F., 2000. Stretch-activated whole cell currents in adult rat cardiac myocytes. Am. J. Physiol. 278, H548–H557.